Mapping the spatiotemporal variability in global storm surge water levels using satellite radar altimetry

Bij de Vaate, Inger; Slobbe, Dirk Cornelis; Verlaan, Martin

DOI
10.1007/s10236-023-01596-2

Publication date
2024

Document Version
Final published version

Published in
Ocean Dynamics

Citation (APA)
Bij de Vaate, I., Slobbe, D. C., & Verlaan, M. (2024). Mapping the spatiotemporal variability in global storm surge water levels using satellite radar altimetry. *Ocean Dynamics*, *74*(3), 169-182. https://doi.org/10.1007/s10236-023-01596-2

Ocean Dynamics
https://doi.org/10.1007/s10236-023-01596-2

Mapping the spatiotemporal variability in global storm surge water levels using satellite radar altimetry

Inger Bij de Vaate[1] · Dirk Cornelis Slobbe[1] · Martin Verlaan[2,3]

Received: 23 December 2022 / Accepted: 23 December 2023

Abstract
Multi-mission satellite altimetry data have been used to study the spatial and temporal variability in global storm surge water levels. This was done by means of a time-dependent extreme value analysis applied to the monthly maximum detided water levels. To account for the limited temporal resolution of the satellite data, the data were first stacked on a **5°** × **5°** grid. Moreover, additional scaling was applied to the extreme value analysis for which the scaling factors were determined by means of a resampling method using reanalysis data. In addition to the conventional analysis using data from tide gauges, this study provides an insight in the ocean-wide storm surge properties. Nonetheless, where possible, results were compared to similar information derived from tide gauge data. Except for secular changes, the satellite-derived results are comparable to the information derived from tide gauges (correlation > **0.5**), although the tide gauges show more local variability. Where limited correlation was observed for the secular change, it was suggested that the satellites may not be able to fully capture the temporal variability in the short-lived, tropical storms, as opposed to extra-tropical storms.

Keywords Storm surges · Sea level · Satellite radar altimetry · Extreme value analysis · Global change

1 Introduction

Coastal zones are densely populated and subject to higher rates of population growth than other regions (McGranahan et al. 2007). At the same time, these regions are extremely vulnerable to many impacts of climate change, one of which is coastal flooding (IPCC 2021). The latter is closely linked to the occurrence of extreme sea level events (ESLs) and observations indicate that such events have increased both in frequency and magnitude (e.g., Oppenheimer et al. 2019; Wahl et al. 2017). Projections suggest this trend to continue in the future (e.g., Oppenheimer et al. 2019). While observations indicate that on the global scale, sea level rise is the primary driver behind the increase in ESLs (e.g., Oppenheimer et al. 2019; Wahl et al. 2017), locally the increase in ESLs may be amplified or even dominated by climate change induced changes in storminess (e.g., Feng et al. 2019; Haigh et al. 2014; Rashid and Wahl 2020).

The strong winds and low atmospheric pressure associated with (extra)tropical storms cause a rise in the water level, a so-called storm surge (Resio and Westering 2008). Several studies suggest that climate change affects the frequency and severity of (extra)tropical storms, which may exacerbate the build up of storm surges in the future (e.g., Calafat et al. 2022; Gori et al. 2022). However, as is stated in the latest IPCC report (IPCC 2021), there is overall low confidence in any observed changes in the frequency or magnitude of storm events and their contribution to ESLs. This is mainly related to the rare and short-lived nature of the storm events and the large local variability (IPCC 2021). The local variability in storm events is particularly important to acknowledge, given that the observational evidence on storm surges predominantly includes in-situ data from tide gauges (e.g., Muis et al. 2016). Hence, the information on storm surge water levels is restricted to coastal regions with an uneven distribution across the globe. Consequently, it is uncertain how storm surges develop at the open ocean or to what extent they are subject to temporal variability on the global scale.

Responsible Editor: Christoph Voelker

✉ Inger Bij de Vaate
i.bijdevaate@tudelft.nl

[1] Civil Engineering and Geosciences, Delft University of Technology, Delft, The Netherlands

[2] Delft Institue of Applied Mathematics, Delft University of Technology, Delft, The Netherlands

[3] Deltares, Delft, The Netherlands

Published online: 30 January 2024

This also affects the validation of global surge models and any predictions that are made using such models.

In this respect, the use of satellite data may provide a significant contribution to our understanding. Over the past decades, measurements of the sea surface height (SSH) have been collected by a series of satellite radar altimeters, providing a record of instantaneous SSH with quasi-global coverage (Adebisi et al. 2021). Although the temporal resolution of satellite altimeters is relatively limited (typical revisit period is 9.9156 days (Beckley et al. 2021)), previous studies have shown that consequent issues may be overcome by combining data from multiple missions and applying data stacking (e.g., citeauthorBdV2021 2021; Cancet et al. 2015). Up to now, a number of studies have been devoted to mapping storm surges using satellite altimetry (e.g., Andersen et al. 2015; Antony et al. 2014; Ji et al. 2019). These studies have shown that with adequate data processing, it is possible to derive comparable storm surge properties from satellite data as from nearby tide gauges. However, in these studies, the analyses were focused on specific geographic regions and it remains uncertain if and how the ability to derive storm surges from satellite data varies globally. This may for instance be due to global differences in the nature of storms (e.g., tropical versus extra-tropical) or global differences in data availability from satellite data. Moreover, the aforementioned examples have not studied temporal changes in storm surges.

Nonetheless, there have been a number of studies on temporal variability in surge (or extreme) water levels using tide gauge data (e.g., Butler et al. 2007; Méndez et al. 2007; Menéndez and Woodworth 2010). And, given the current record of satellite radar altimetry, it should theoretically be possible to apply similar methods to study temporal variability in surge water levels from satellite data. In fact, this has already been demonstrated by Lobeto et al. (2018) who successfully used satellite altimetry to study the time-dependency in extreme sea levels, albeit on a local scale (along the North American East Coast). In their study, a scaling factor was used, to account for the irregular sampling of satellites. This use of scaling is not new, e.g., Izaguirre et al. (2011) applied a similar method to derive global wave height variability from satellite altimetry. In this paper, we build upon these previous studies and apply a time-dependent extreme value analysis, including location-specific scaling, to satellite radar altimeter-derived surge water levels. We present a full ocean-wide mapping of quasi-global storm surge water levels and their time variability. Here, we focus both on annual variation and secular changes in the magnitude of storm surge water levels. In addition, results are compared to similar information derived from a global tide gauge data set. In the following sections, we first give an outline of the data used in this study, before introducing the methodology and discussing the results.

2 Data

2.1 Satellite radar altimetry

This study exploited data from eight low-resolution mode (LRM) satellite radar altimeters, that are: TOPEX/Poseidon and Jason 1–3 (further referred to as TPJ), ERS-1 and ERS-2, Envisat-1 and SARAL (see Fig. 1). The data were combined for the full span of the TPJ-satellites (considering full years), resulting in 29 years of sea level data (1993–2021). All altimeter data were obtained through the Radar Altimeter Data System (RADS; (Naeije 2022)). The surge water levels were computed as follows:

$$WL_{surge} = H - R_{obs} - MSS - \textit{geophysical and range corrections} \quad (1)$$

where H represents the altitude of the satellite with respect to the WGS84 ellipsoid, R_{obs} the measured range between the satellite and the surface, and MSS the vertical datum, being the DTU18-Mean Sea Surface product (Andersen et al. 2018). The following geophysical and range corrections were applied: the ionosphere (NIC09 for TOPEX/Poseidon and ERS-1, GIM for others), dry troposphere (ECMWF), wet troposphere (if available: radiometer, otherwise: ECMWF), the solid tide (Cartwright and Edden 1973; Cartwright and Taylor 1971), pole tide (Wahr 1985), ocean tide and load tide (FES2014), sea state bias (BM3 for ERS-1 and ERS-2, Tran et al. (2018) for SARAL/AltiKa and CLS for all others), and the reference frame offset.

Data from all satellites were stacked on a rectangular lat/lon grid with variable dimensions (see Sect. 3.2). Subsequently, additional processing of the water levels was required to remove outliers. While this is typically done using a multiple of the standard deviation of the time series as upper and lower boundary (e.g., Dinardo et al. 2018; Kleinherenbrink et al. 2015), this may in our case also remove the (more extreme) surge water levels. Hence, we opted for a alternative approach using the dynamic atmosphere correction (MOG2d (ERA Interim forcing)). Here, data were classified as outliers when their absolute deviation from the median exceeded three times the 5-day moving maximum of the dynamic atmospheric correction. This dynamic approach adequately accounts for the spatiotemporal differences in water level variability. Finally, to be able to isolate the effect of variability in storminess on the ESLs, the yearly mean sea level was removed from the time series by subtracting their 365-day moving mean. Note that the remaining water level may still reflect other processes (e.g., baroclinity or non-linear interactions between tides and surges), but these

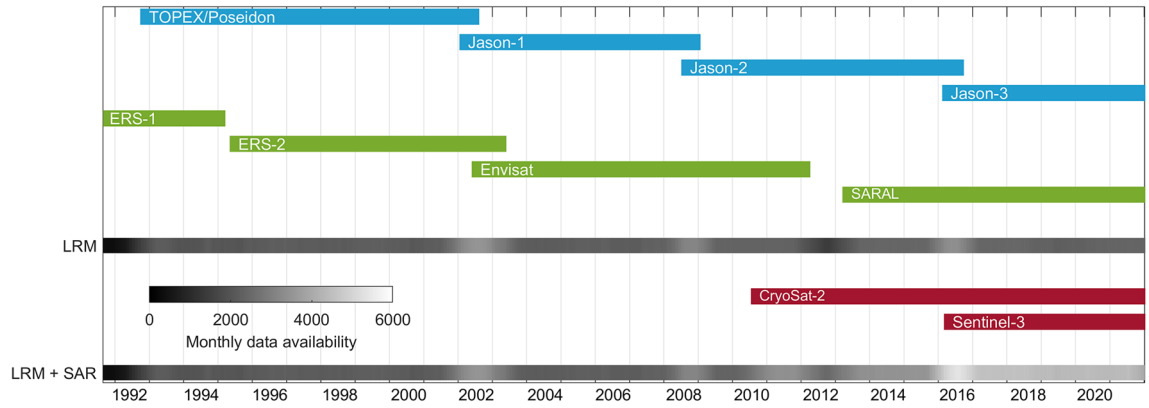

Fig. 1 Schematic of satellite radar altimeter data availability over time, excluding interleaved phases for the conventional LRM and the LRM and synthetic aperture radar (SAR) missions combined. Note that this is an example based on a 5° × 5° area in the North Sea and that the absolute number of data points varies across the globe. Data from the higher resolution SAR altimeters, CryoSat-2 and Sentinel-3, were excluded from this study to ensure largely consistent data availability throughout the studied time span

were assumed to be negligible compared to the actual surge variability.

2.2 Tide gauges

Alongside the altimeter data, data from a selection of tide gauges (obtained from the GESLA-3 dataset (Haigh et al. 2022)) were processed to allow for a comparison of the derived surge properties. For this purpose, we only considered tide gauge data from the period for which satellite altimeter data was available (1993–2021). The temporal resolution of the tide gauge data varies from one minute to one hour, mainly depending on the country where the stations are located and the time of data acquisition. In contrast to the altimeter data, the tide gauge data were detided using tidal constants obtained by means of harmonic analysis using the UTide-software (Codiga 2020) instead of using FES. This was done to remove as much of the tidal signal as possible, thus including (shallow water) tides that are not in FES but may be significant at the location of most tide gauges. Finally, the time series was referenced to the annual mean sea level by subtracting the 365-day moving mean from the time series.

2.3 Reanalysis data

Reanalysis data were used to compute scaling factors to account for the limited temporal resolution of the satellite-derived water levels (as described in Sect. 3.2). These data were obtained from the Global Tides and Surge Model (GTSM, Wang et al. 2021; Muis et al. 2016), forced by ERA5 reanalysis data. GTSM is a barotropic (2D) model that runs on an unstructured grid with a resolution that increases from 25 km on the open oceans to 2.5 km at the coast. GTSM has previously been used for a global reanalysis of storm surge water levels, where validation using observed time series at tide gauges resulted in an average RMSE of only 0.11 m (Muis et al. 2016). In this study, time series with a sampling rate of 10 minutes were reconstructed for the full TPJ period. This was done for over 600 locations covering the global oceans. Subsequently, the time series were detided and referenced to the annual mean sea level in a similar way as was done with the tide gauge data.

3 Methods

3.1 Extreme value analysis

Earlier studies that used satellite radar altimetry to observe storm surges typically used a so-called peak-over-threshold (POT) approach to identify single surge events that exceed a given magnitude (Andersen et al. 2015; Antony et al. 2014; Ji et al. 2019). While this is a common approach in extreme value analysis, its use in the presented study would have one important drawback. Namely, the POT approach relies on a threshold that is defined a priori, and can thus not easily be used to study temporal and spatial variability in surge water levels (as this would require setting separate thresholds for different locations and periods (Butler et al. 2007)). Another approach that has been used in storm surge analyses is the so-called block-maxima approach (e.g., Butler et al. 2007; Muis et al. 2016). Such an approach relies on a relative definition of an extreme value (with respect to other water levels in the specified block) and can thus be unambiguously applied to records with varying magnitudes of variability (Butler et al. 2007). Similar to studies by Méndez et al. (2007); Menéndez and Woodworth (2010); Lobeto et al. (2018) on ESLs, we opted for the use of monthly maxima surge water levels (*MM*)

to be able to resolve annual differences. Moreover, the use of monthly blocks results in a larger number of data points (compared to annual blocks) and thus compensates for the limited record of satellite data. On the other hand, the blocks are still of sufficient length with respect to the poor temporal resolution of the data (compared to e.g., weekly blocks).

Subsequently, as was also done in the aforementioned studies, a time-dependent Generalized Extreme Value Distribution (GEVD) was fitted to the series of *MM*. The GEVD (Eq. 2) is a three-parameter distribution where F represents the cumulative probability associated with *MM*, μ is the location parameter, σ the scale parameter, and ξ the shape parameter. Depending on the shape parameter, the GEVD can belong to the Weibull, Gumbel or Fréchet family (Lobeto et al. 2018). In addition, inspired by Izaguirre et al. (2011); Lobeto et al. (2018), scaling was introduced in the distribution to account for the poor temporal sampling by the satellites. Where undersampling of the water level by the satellites would almost always result in an underestimation of the *MM*, the degree of underestimation depends on the actual data availability. This in turn is related to the resolution of the stacking grid, the configuration of the satellite tracks, and topography. Therefore, globally variable scaling was used to correct the underestimation (see Sect. 3.2 for more details). In contrast to the aforementioned studies, we opted for two scaling factors: k_1 for the location parameter and k_2 for the scale parameter. This decision stemmed from experimental analysis using artificial data, that indicated that undersampling results in a bias in the average *MM*, but also affects the spread of the *MM*'s. Hence adopting two scaling factors would allow for a better representation. Ultimately, this resulted in the following GEVD:

$$F(MM) = \begin{cases} \exp(-[1+\xi(\frac{MM-k_1\mu(t)}{k_2\sigma(t)})]^{-\frac{1}{\xi}}) & \xi \neq 0 \\ \exp(-\exp[-(\frac{MM-k_1\mu(t)}{k_2\sigma(t)})]) & \xi = 0 \end{cases} \quad (2)$$

Here, the temporal variability was included in $\mu(t)$ and $\sigma(t)$ as follows, where $\omega = 2\pi$ year^{-1} and t is given in years with respect to the center time of the considered data. $\alpha_{[0,1,2,3]}$ and $\beta_{[0,1,2,3]}$ were estimated:

$$\begin{aligned} \mu(t) &= \alpha_0 + \alpha_1 t + \alpha_2 \cos(\omega t) + \alpha_3 \sin(\omega t) \\ \sigma(t) &= \beta_0 + \beta_1 t + \beta_2 \cos(\omega t) + \beta_3 \sin(\omega t) \end{aligned} \quad (3)$$

The model parameters were estimated by means of the maximum likelihood method as described in Méndez et al. (2007). The scaling factors (k_1 and k_2) were determined a priori based on experiments with the reanalysis data (see Sect. 3.2). In addition to satellite data, high-frequency data from tide gauges were processed in a similar manner as the satellite data, except for the scaling factors, which now were excluded from the GEVD.

3.2 Data availability and scaling factors

Despite that we have used satellite data from multiple missions and stacked the data over larger areas, it is likely that not all storm surges were captured in full magnitude. To account for this, two scaling factors were introduced in the GEVD. Since we considered that the predominantly coastal tide gauge data would not be representative for ocean-wide surge variability, the values of these scaling factors were determined by means of global reanalysis data. For this purpose, the model-derived time series, introduced in Sect. 2.3, were randomly sub-sampled following the location-specific satellite sampling distribution. To improve the accuracy of the estimated scaling factors, this was done 25 times (as a compromise between achieved accuracy and computation time), resulting in 25 different realizations of the time series. For each realization, the *MM* were computed and the GEVD was fitted to the data while including the scaling factors k_1 and k_2. The optimal scaling factors were determined by minimizing the root-mean-square-error (RMSE) between the GEVD based on the original high-frequency data and the GEVD based on the sub-sampled data. Finally, the optimal, location-specific, scaling factors were computed as the median of values resulting from the 25 realizations. At the same time, the standard error (SE) of these scaling factors was computed as 1.4826 times the median absolute deviation of the 25 values. This experiment was done for two different grid sizes ($2° \times 2°$ and $5° \times 5°$) to gain insight in the impact of the size of the area over which satellite data were stacked, on the ability to accurately capture storm surge dynamics. Note that the precise satellite sampling and data availability also varies across the globe as the satellite tracks converge towards the poles, while on the other hand, the metric distance between longitudes reduces towards the poles and the (seasonal) presence of sea ice may hamper measurements of the sea level.

To assess the use of reanalysis data for the computation of the scaling factors on open ocean, the same procedure was carried out using a selection of tide gauges that were located at least 100 km from the continental coastlines. Only tide gauges were used that have at least multiple years of gapless data. To prevent the validation from being affected by temporal differences in storm surge magnitude, the reanalysis time series were first trimmed to the exact time span of the tide gauge time series. However, note that the time spans of the available data vary per tide gauge, hence truncating the time series may introduce additional spatial variation in obtained scaling factors.

3.3 Storm surge characteristics

From the estimated location, scale, and shape parameters, the storm surge water levels for certain return periods of interest were calculated by means of the inverse of Eq. 2, excluding the scaling factors:

$$MM_T = \begin{cases} \mu - (\frac{\sigma}{\xi}[1 - (-\ln[1 - \frac{1}{T*12}])^{-\xi}]) & \xi \neq 0 \\ \mu - \sigma \ln(-\ln[1 - \frac{1}{T*12}]) & \xi = 0 \end{cases} \quad (4)$$

where T is the return period in years. The term $1 - \frac{1}{T*12}$ represents the probability that MM will be below or equal to MM_T, hence the term equals the cumulative probability (F) from Eq. 2. In this paper the surge MM water levels are shown for a return period of $\frac{1}{6}$ years and for 10 years, these will be referred to as the $MM_{\frac{1}{6}}$ and MM_{10} respectively (where the subscript denotes the return period). These specific periods were chosen because a return period of $\frac{1}{6}$ years corresponds to a cumulative probability of 0.5 (namely $1 - \frac{1}{\frac{1}{6}*12} = \frac{1}{2}$), hence it equals the average MM. On the other hand, the 10-year return period represents a more extreme case, while still remaining well within the time span of the data availability, ensuring reasonable uncertainties.

Since we considered a time-dependent GEVD, the values for μ and σ were first computed based on the fitted α- and β-parameters and t. This allowed for a reconstruction of a time-varying series of MM_T -values from which the surge characteristics of interest were derived. In this paper the following characteristics are studied: time-averaged MM_T, annual range (the difference between the highest and lowest MM_T in the year, excluding the secular change), annual phase (month with highest MM_T) and the secular change (linear trend in MM_T).

4 Results

4.1 Data availability and scaling factors

The number of data from satellite altimeters that were available per grid cell roughly equaled 2.5×10^5 from 40° S to 40° N, but then increased to 3×10^5 at 60° N/S, for the coarse (5° × 5°) grid. Using the fine (2° × 2°) grid, reduced the data availability by about 83%. In addition, as mentioned before, the sea-ice affected regions experience seasonal differences in data availability. This likely affected the derived storm surge properties. For this reason, all figures showing satellite data-based results will also show the maximum sea ice extent during the TPJ period (derived from NSIDC (2022)), as a reminder to treat these specific results with caution.

The obtained optimal scaling factors for the coarse grid (5° × 5°) are shown in Fig. 2a and d. Overall, the location parameter (μ) required more scaling in the tropics (i.e., scaling factor k_1 deviates more from 1), compared to higher latitudes. This relation is less obvious for scaling factor k_2. Moreover, the average SE for k_1 and the average RMSE of the obtained GEVD showed a clear latitude dependency, with larger errors at higher latitudes. In addition, as a result of the lower data availability, the analysis on the fine grid required more scaling than when the coarse grid was used (Fig. 2b, e). Nonetheless, the analysis on the fine grid resulted in significantly larger errors than the analysis on the coarse grid (Fig. 2c). Based on these results, it was decided to use the coarse grid for the remainder of the study.

The main findings from the comparison with scaling factors computed from tide gauge data are presented in Fig. 3. For the majority of the locations, the differences between the obtained scaling factors were within the 95%-confidence intervals of these differences and were thus considered to be insignificant (particularly applied to k_2, Fig. 3d). For k_1, the significant differences mainly concerned higher scaling factors derived from the tide gauges compared to those derived from GTSM, except for some locations in the Pacific Ocean (Fig. 3a). This implies that the derived surge water levels would be scaled up more when considering the GTSM-based product (as a lower scaling factor corresponds to increased scaling). However, for k_2, all significant differences concerned lower scaling factors derived from the tide gauges compared to GTSM (Fig. 3d, f). For the majority of the locations, better scaling results were obtained in the analysis of reanalysis data: that is, the RMSE between the GEVD based on the original high-frequency and satellite-sampled data was lower. This particularly applied to the locations where the tide gauge-derived k_1 exceeded the GTSM-derived k_1 (Fig. 3b). Comparing the absolute values (Fig. 3c, f) shows larger variability in the tide-gauge derived scaling factors. The coefficient of determination (r^2) is only 0.26 and 0.19 for k_1 and k_2 respectively.

Figure 4 visualizes the consequences of using the coarse grid as opposed to the fine grid by comparing the obtained time-averaged $MM_{\frac{1}{6}}$ and MM_{10} to information derived from tide gauges. The message is two-fold: (1) using the coarse grid resulted in more spatial data gaps when a significant portion of a grid cell covered land and was omitted and (2) using the coarse grids resulted in more averaging of the surge water levels. This generally resulted in lower values compared to tide gauges as ESLs tend to increase towards the coast. The latter can be clearly seen the North Sea. However, the opposite effect was observed in the Skagerrak (the water between Norway and Denmark) where the fine grid resulted in lower values than the coarse grid.

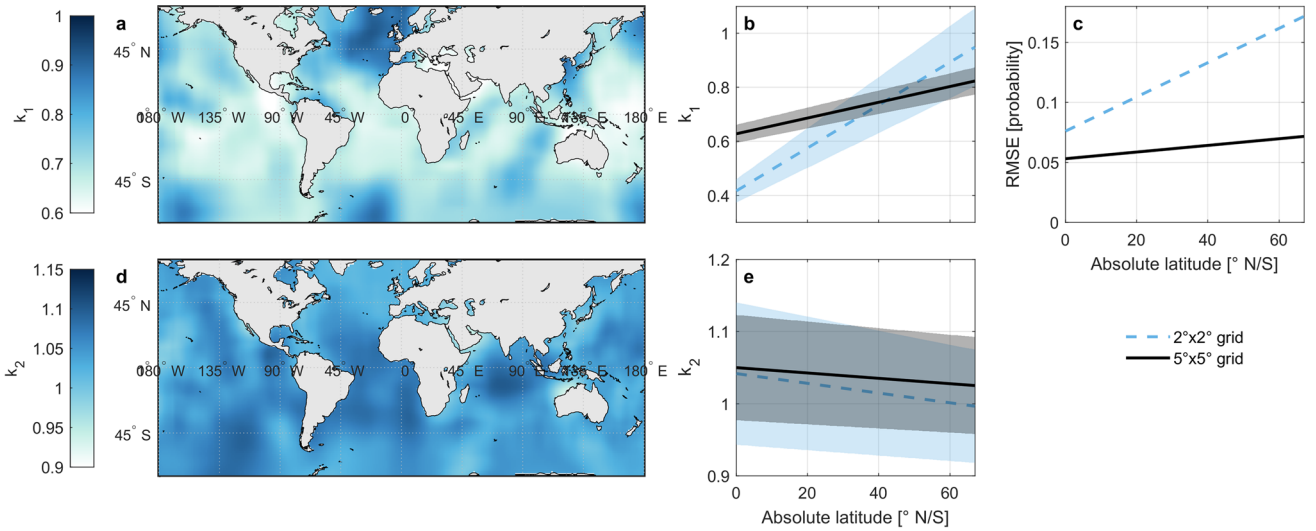

Fig. 2 Global estimates of the scaling factors k_1 (**a**) and k_2 (**d**) for the analysis on the coarse grid (5° × 5°). Note the difference in color scales used for the two subfigures. The average scaling factors k_1 (**b**) and k_2 (**e**) including their standard error (patched area) are shown as a function of absolute latitude (linear fit), as well as the RMSE between the GEVD based on the original high-frequency and satellite-sampled data (**c**), for both the fine (2° × 2°) and coarse grid

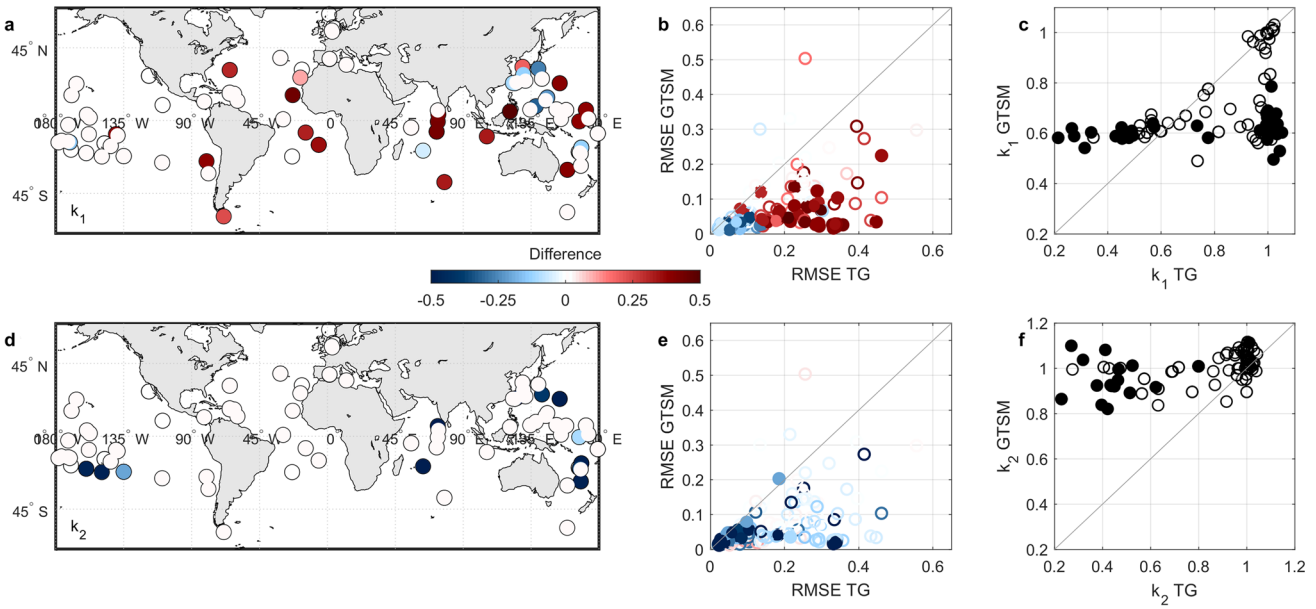

Fig. 3 Difference between the scaling factors k_1 (**a**) and k_2 (**d**) obtained from tide gauge (TG) and reanalysis (GTSM) data for the secular analysis on the coarse grid (5° × 5°). Positive values (red) indicate the tide gauge-derived factor is larger. Insignificant differences (i.e., that do not exceed the 95% confidence interval of the difference) have been colored white. Difference between the scaling factors k_1 (**b**) and k_2 (**e**) as a function of the RMSE between the GEVD based on the original high-frequency and satellite-sampled data. Absolute values for the scaling factor k_1 (**c**) and k_2 (**f**) derived from tide gauge and reanalysis data (GTSM). Filled scatters indicate significant differences between the two scaling factors

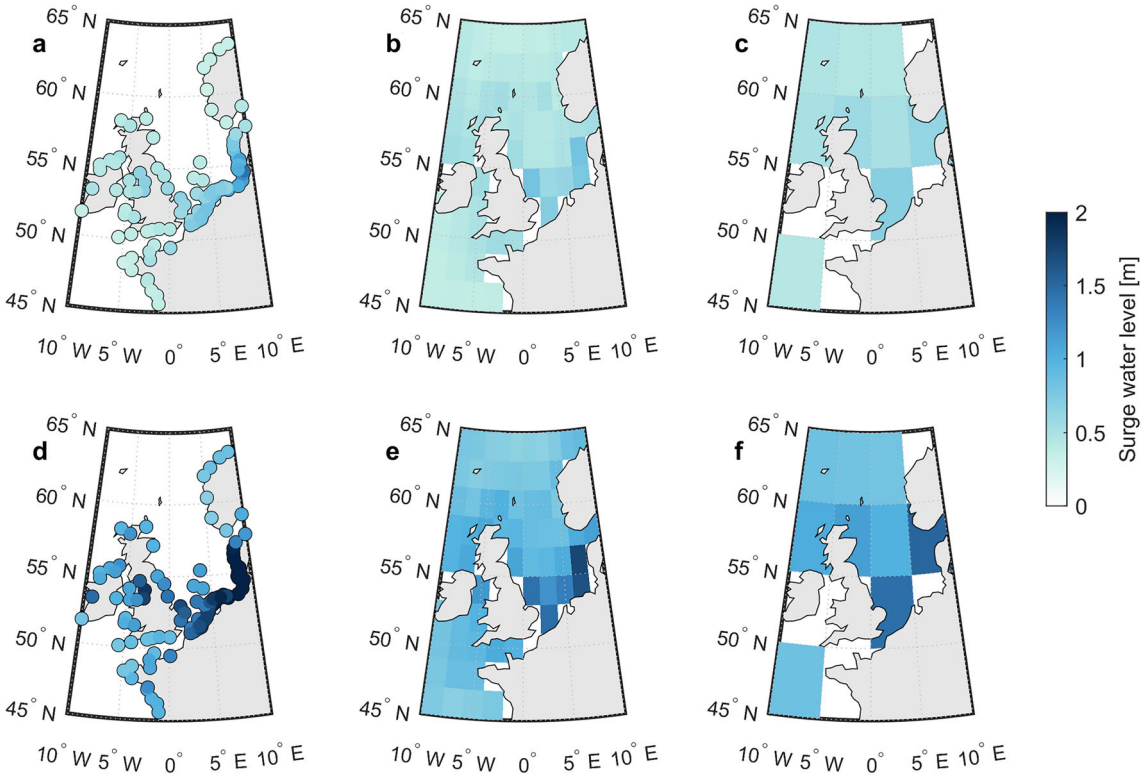

Fig. 4 Time-averaged $MM_{\frac{1}{6}}$ (**a**, **b**, **c**) and MM_{10} (**d**, **e**, **f**) following from tide gauge data (**a**, **d**), the satellite data stacked on the fine grid (2° × 2°; **b**, **e**) and the satellite data stacked on the coarse grid (5° × 5°; **c**, **f**)

4.2 Time-averaged surge water levels

The time-averaged $MM_{\frac{1}{6}}$ and MM_{10} are visualized in Fig. 5a and b, respectively. Both quantities showed a strong zonal dependency with lower values in the tropics (about 0.25 m for both return periods) and larger values at mid and high latitudes (about 0.6 and 1.2 m respectively). This pattern was observed in both the satellite-derived and the tide gauge-derived products. More increased surge water levels compared to their surroundings were observed in the northwest Atlantic Ocean, the northwest Pacific Ocean, and the Southern Ocean. In several instances, the surge water level at one tide gauge exceeded that of surrounding tide gauges and the nearby satellite-derived product (e.g., in the Gulf of Mexico and the North Sea). In addition, higher surge water levels were observed in the sea-ice affected regions, particularly in the Southern Ocean. Overall, the 95%-confidence intervals related to both yearly average MM_T's (not shown) are narrow ($< 0.3MM_T$ for 95% of the grid cells), with the exceptions being located in the sea-ice affected regions. The correlation between the tide gauge-derived product and the satellite-derived product (interpolated to the locations of the tide gauges) was computed as 0.63(±0.04) for $MM_{\frac{1}{6}}$, and 0.67(±0.04) for MM_{10}.

4.3 Annual differences in surge water levels

As shown in Fig. 6a and b, storm surges water levels on the northern hemisphere were subject to significant annual variation (up to 0.4 m for $MM_{\frac{1}{6}}$ and 0.75 m for MM_{10}), while this was much less for the storm surges on the southern hemisphere (up to 0.2 m for $MM_{\frac{1}{6}}$ and 0.4 m for MM_{10}). Here, the sea-ice affected region in the Southern Ocean appeared to be a clear outlier with an annual range in both $MM_{\frac{1}{6}}$ and MM_{10} of 0.75 m or more. For the majority of the domain (95% of the grid cells), the 95%-confidence intervals related to the annual ranges (not shown) subceed the annual ranges ($< 0.7MM_{\frac{1}{6}}$ and $< 0.95MM_{10}$), with the exceptions again being located in the sea-ice affected regions.

Overall, the annual phase (the month with the highest MM_T) was found to correspond to the local winter (Fig. 7). Exceptions were predominantly located in the tropical zone, e.g., the Japanese and Philippine Seas (August) and the Arabic Sea (July). Another striking region was the zonal band in the Pacific Ocean around 15° N where the $MM_{\frac{1}{6}}$ was largest in March/April. Moreover, while the overall pattern in the annual phase is comparable for $MM_{\frac{1}{6}}$ and MM_{10}, that of MM_{10} showed more variability in the tropics. Finally, the annual phase of the MM in sea-ice affected regions cor-

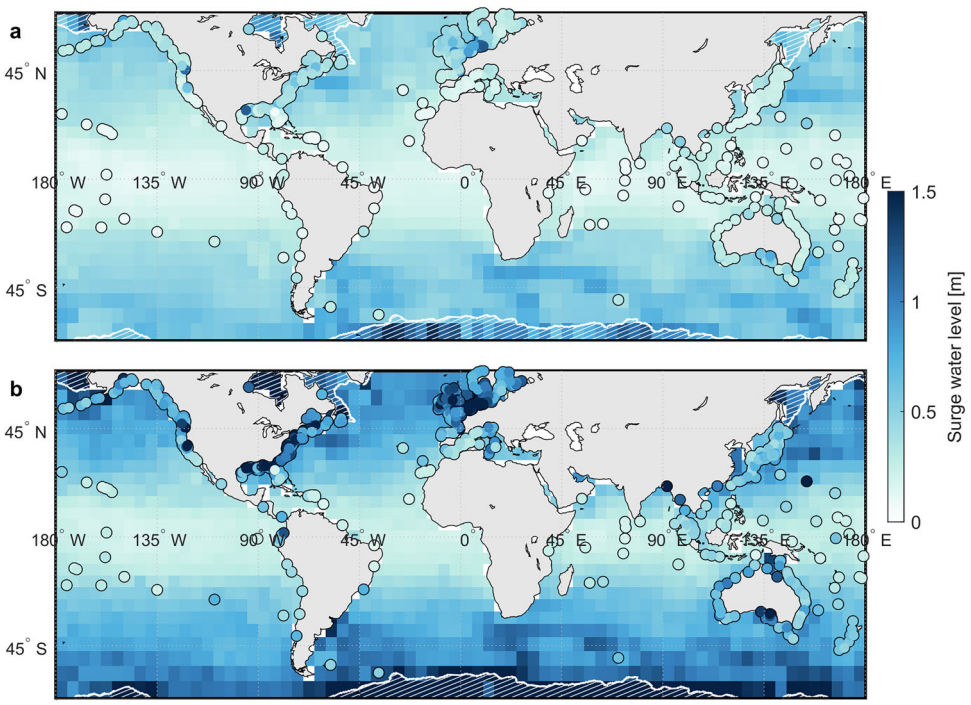

Fig. 5 Time-averaged $MM_{\frac{1}{6}}$ (**a**) and MM_{10} (**b**) following from the satellite data (background) and tide gauge data (scatters). The hatched regions indicate the maximum sea ice extent during the TPJ period

responds to the month of maximum sea ice extent (March for the northern hemisphere and September for the southern hemisphere).

The computed correlation coefficient between the satellite-derived product and that from tide gauges was 0.57(±0.04) (0.73(±0.03)) for the annual range of $MM_{\frac{1}{6}}$ (MM_{10}) and 0.53(±0.04) (0.50(±0.04)) for the annual phases. Differences were predominantly observed along the west coast of North America (annual range of MM_{10}), in the Arabic Sea (annual phase), and Gulf of Mexico (all variables).

4.4 Secular change surge water levels

Global changes in the $MM_{\frac{1}{6}}$ of ∼ 0.25 cm/year were derived across the globe (Fig. 8a). The trend was predominantly negative, while several mid-latitude regions showed an increase instead. In contrast to the earlier studied variables, the trend estimates only exceed the associated 95%-confidence intervals (Fig. 8b) in ∼40% of the grid cells. The 95%-confidence intervals exhibit a similar zonal pattern as the time-averaged MM_T's; larger uncertainties in the trend estimates were found in the subtropics, where the time-averaged MM_T's were highest (Fig. 5). Moreover, there was poor agreement between tide gauges- and satellite-derived yearly trends: the computed correlation coefficient was 0.11(±0.06). An example of a region where there was a consistent mismatch between the tide gauge- and satellite-derived change in $MM_{\frac{1}{6}}$ is the east coast of North America. As this region knows the frequent occurrence of tropical storms (see Fig. 9), the correlation coefficient was again computed considering only the tide gauges that are located outside of the areas that are affected by tropical storms. This resulted in a higher correlation, namely: 0.28(±0.07). The mismatch appeared to be partly related to the high local variability in the tide gauge-derived change or isolated tide gauges (e.g., the tide gauges in the western Pacific that show positive trends). In fact, filtering out spatial outliers from the trends derived at tide gauges,[1] increased the correlation up to 0.35(±0.08) for a distance of 200 − 220 km. The correlation reduced again for larger distances. This relation was also observed for the time-averaged MM_T and annual variation variables, albeit with some differences in the optimal distance. Finally, large negative trends (exceeding 0.5 cm/year) were observed in the sea-ice affected regions.

5 Discussion

For the first time, the vast amount of data available from satellite radar altimeters has been used to map the temporal variability in global storm surge water levels. This has been done by fitting a time-dependent generalized extreme value distribution (GEVD) to the monthly maximum (MM) surge water levels. However, in contrast to the in-situ data that have been widely used to study storm surges, the data from satellite altimeters have a rather coarse temporal res-

[1] defined as locations where the trend deviates more than two times the MAD from the median trend computed over all tide gauges within a certain distance.

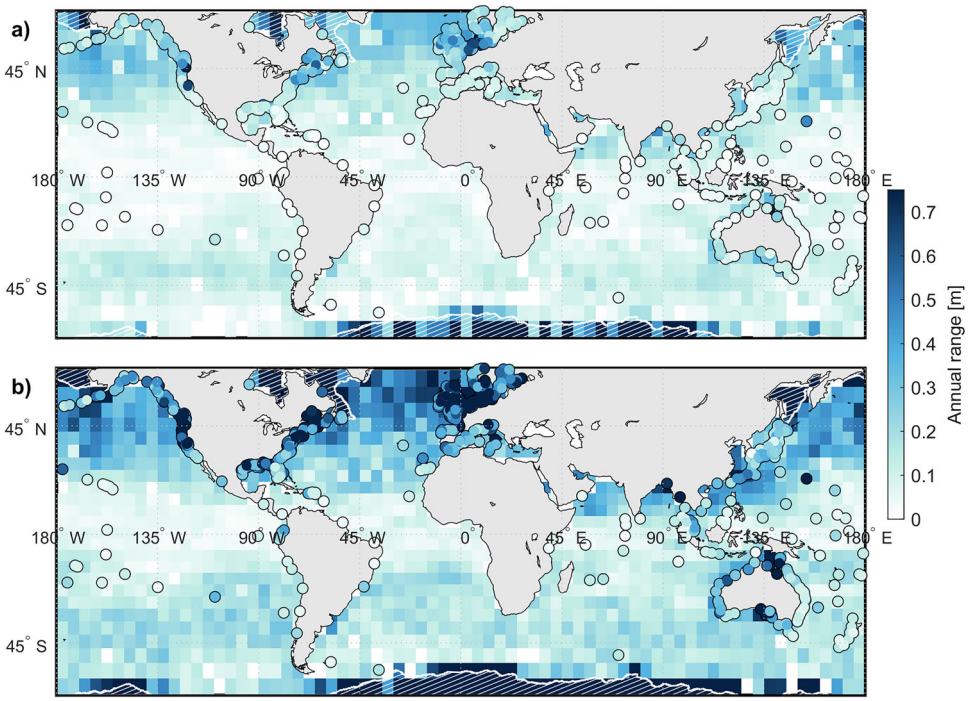

Fig. 6 Annual range in $MM_{\frac{1}{6}}$ (**a**) and MM_{10} (**b**) following from the satellite data (background) and tide gauge data (scatters). The hatched regions indicate the maximum sea ice extent during the TPJ period

olution. To ensure sufficient coverage of storm events, the measurements from eight different missions were combined and stacked over areas of 5° × 5°. In addition, an experiment based on reanalysis data was performed to obtain location-specific scaling factors that correct for possible bias in storm surge water levels obtained by the satellites. Subsequently, the time-average storm surge water levels and their annual variation and secular change were derived and compared to the same information derived from high-frequency tide gauge data.

The main findings presented in this paper are the following. The time-average $MM_{\frac{1}{6}}$ and MM_{10} showed a clear zonal pattern, with higher water levels observed at mid and high latitudes compared to the equatorial region. The largest

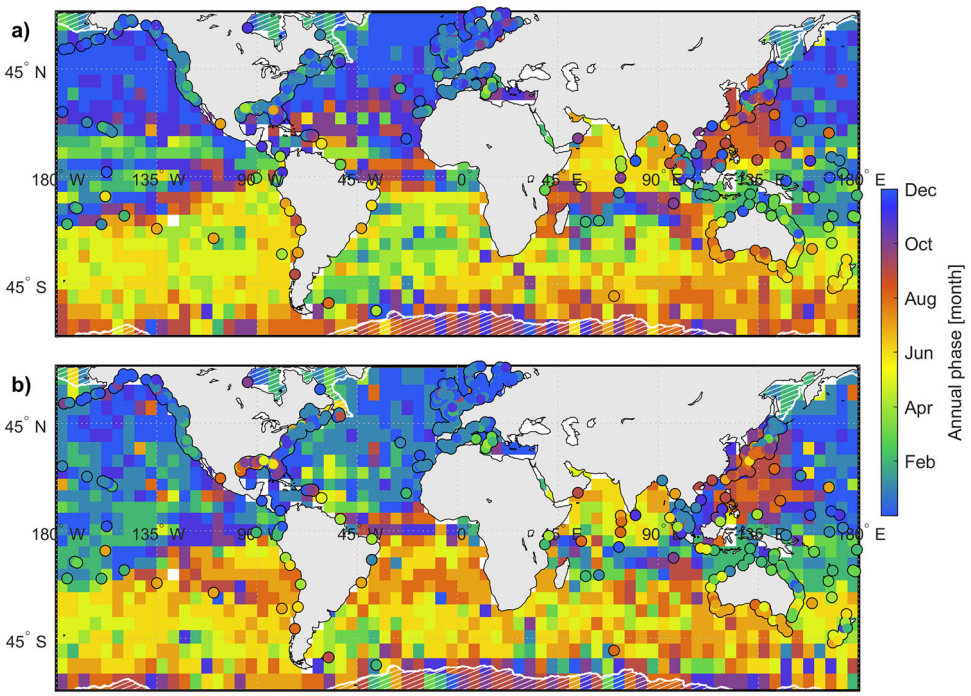

Fig. 7 Annual phase of (month with the highest) $MM_{\frac{1}{6}}$ (**a**) and MM_{10} (**b**) following from the satellite data (background) and tide gauge data (scatters). Locations with insignificant annual variation have been left white. The hatched regions indicate the maximum sea ice extent during the TPJ period

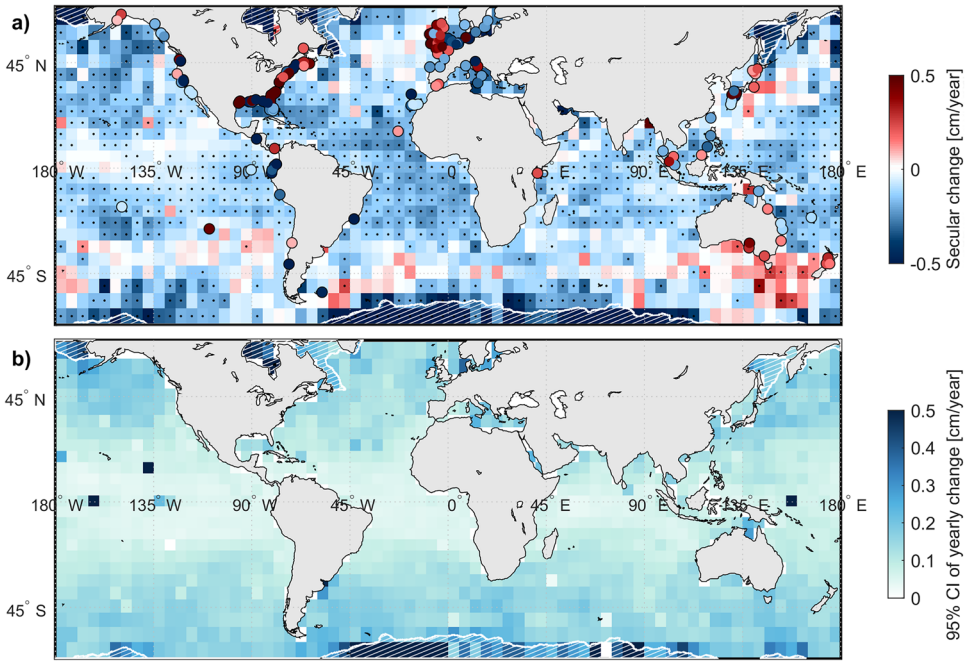

Fig. 8 Yearly trend in $MM_{\frac{1}{6}}$ following from the satellite data (background) and tide gauge data (scatters) (**a**). Only satellite-derived trends that exceed the 95% confidence interval have been dotted. Tide gauge-derived trends that were insignificant at the 95% confidence level were excluded from the plot. The 95% confidence intervals are shown in (**b**). The hatched regions indicate the maximum sea ice extent during the TPJ period

storm surge water levels were observed in the northwest Atlantic Ocean, northwest Pacific Ocean, Southern Ocean and North Sea. These regions correspond to regions where the mesoscale variability is large (e.g., Rhines 2001). As the mesoscale variability has not been removed from the "surge" water levels, it is unknown to what extent this affects the larger magnitude in the aforementioned regions. However, these regions do not stand out when considering the temporal variability in storm surge water levels. The annual variation in the storm surge water levels was particularly large at mid to high latitudes in the northern hemisphere. The largest annual variation was observed in the sea-ice affected regions, although there are reasons to question that finding (more will follow). While the month in which the highest surge water levels were observed generally corresponds to the local winter, in particular in the tropics, there were some exceptions. Most likely, this is related to the nature of the storms that are captured. Where extra-tropical storms typically occur in winter, tropical storms (i.e., hurricanes, cyclones, and typhoons) have a different seasonality (e.g., peak activity in September for the North Atlantic, in August for Japan (Camp et al. 2015)). Lastly, a predominant negative trend in storm surge water levels was observed across the domain, except for certain regions at mid-latitudes. Although the uncertainties associated with the time-averaged *MM*'s and annual variation were generally small, they were more significant for the trend estimates. In many cases ($\sim$ 60%) the trend estimate did not exceed its 95%-confidence interval.

The results derived from the satellite data have been compared to a similar product derived from tide gauges. This comparison can be used to assess the ability to use satellite data for storm surge analysis. However, it should be kept in mind that one cannot expect a perfect agreement between the products derived from both data sources. Firstly, the tide gauge data are point estimates, while the satellite product is a spatial average. As was seen in Fig. 4, the obtained quantities closely depend on the size of the area that was used for stacking of the satellite data. In addition, not all tide gauge data cover the full TPJ period, nor are they gapless. Consequently, given the high interannual variability in storminess

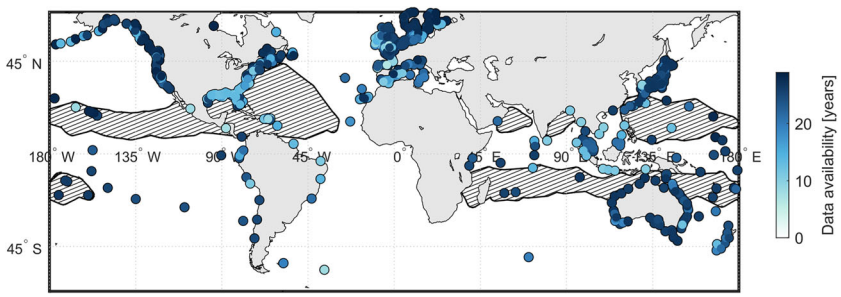

Fig. 9 Number of years with data for tide gauges used in the study. The hatched regions indicate the areas that are affected by tropical storms with wind speeds exceeding 100 knots (derived from Knapp et al. (2022))

(IPCC 2021; Weisse et al. 2014), the secular changes derived from the tide gauges may not be representative for the full TPJ period.

Nevertheless, a reasonable agreement between the tide gauge and satellite-derived product was observed for the time-average and annual properties. However, more contradictions were observed for the secular change. As mentioned, this may be related to the data availability at the tide gauges, although this mainly affects the tide gauges in Southeast Asia and the Gulf of Mexico (Fig. 9), while contradictions were also observed elsewhere. Hence, two alternative reasons are suggested. Firstly, the secular results appeared to be more dominated by local variability and it is plausible that the change in storminess at the coast of one island in e.g., the Pacific Ocean is not representative for the 5° × 5° area that this island is located in. This is supported by the fact that excluding spatial outliers from the trends derived at tide gauges resulted in better correlation. On the other hand, a positive trend in $MM_{\frac{1}{6}}$ was observed at a number of tide gauges along the east coast of the USA, yet not captured by the satellite-derived product. This leads to the second hypothesis concerning the difference between tropical and extra-tropical storms. Tropical storms are typically shorter and smaller than extra-tropical storms (Von Storch and Woth 2008) and therefore more likely to be missed by the satellite data. The latter is supported by the fact that the annual phase of the $MM_{\frac{1}{6}}$ and MM_{10} did not everywhere correspond to the local season of tropical storms (Camp et al. 2015), even though tropical storms surges typically have a larger amplitude than extra-tropical storms (Von Storch and Woth 2008). The contradictions in observed trends along the east coast of the USA suggest the positive trend may reflect changes in the tropical storms as opposed to a background negative trend in extra-tropical storms. However, the regional increases in storm surge water levels around 45° N/S are consistent with the observed poleward shift in tropical storms (IPCC 2021).

Another apparent limitation of the satellite data is related to the sea-ice affected regions. All studied storm surge properties show rather extreme values in the regions that are affected by sea ice that may not be an actual representation of the truth. Similarly, in these regions the uncertainties associated with the estimated parameters appeared exceptionally large. The derived annual phase and secular change suggest that the results in these regions are affected by contamination from reflections of the sea ice rather than the actual water level. Namely, the annual phase corresponds to the period of maximal sea ice extent (September for the Antarctic and March for the Arctic (NSIDC 2022)), and in this season one would not expect a significant surge as the water surface can only to a limited extent be disturbed by the wind. If, however, the data is dominated by reflections from the sea ice, a higher "water" level is indeed expected during months with maximal sea ice extent. In addition, the negative trend in surge water levels in the regions suggests contamination by sea ice reflections. As the sea ice extent reduces over time, the contamination would also reduce, resulting in a reduction in extreme "sea" level measurements. In fact, the sea-ice affected regions would be an interesting study area, precisely because of the significant changes to the sea ice extent. However, for such a study, a more explicit selection of the radar returns is required.

Furthermore, the method of obtaining scaling factors using reanalysis data has been assessed by comparison to a similar analysis using data from a selection of tide gauges (Fig. 3). Overall, a larger spread was observed in the scaling factors derived from tide gauge data compared to the reanalysis data (Fig. 3c, f). In most locations, the differences between the factors derived from the reanalysis and the tide gauge data appeared insignificant. For k_2, only a few significant differences were found, predominantly in regions that are affected by tropical storms (see Fig. 9). In all of these cases, the factors derived from the reanalysis data exceed those derived from the tide gauge data. This suggests that the obtained surge water levels may be scaled too little. On the other hand, in several instances, significantly lower values (thus more scaling) were computed from the reanalysis data for scaling factor k_1. Although, as this predominantly concerns locations where the scaling is significantly less successful in the experiment with tide gauge data compared to that with reanalysis data (higher RMSE, Fig. 3b), this questions the reliability of the tide gauge-derived scaling factors.

Unfortunately, a comparison of the results presented in this paper to findings by earlier studies is not straightforward, for various reasons. First of all, many studies on changes in extreme sea level events (ESLs) do not exclude the impact of variability in the mean sea level (MSL) (e.g., Wahl et al. 2017; Weisse et al. 2014). In contrast, the study by Menéndez and Woodworth (2010) (and a follow-up by Marcos and Woodworth (2018)) specifically attempted to distinguish the impact of the MSL on the temporal variability in ESLs derived from tide gauge records. While by including the MSL an overall increase in ESLs was observed across the globe, the observed change was predominantly negative when the MSL was excluded. Although this corresponds to the findings presented in our study, some contradictions were observed for individual tide gauges. Consequently, a second issue that complicates intercomparisons of results was identified: the timespan of considered datasets. Since the study by Menéndez and Woodworth (2010) was mainly based on tide gauge data from 1970 up to 2010, it is unknown to what extent any differences in results are related to the high interannually variable character of storm surges. On another note, the seasonal pattern found in their study did largely correspond to what was presented in this paper. Finally, while the presented

analysis provides a range of information on storm surge water levels and their temporal variability, it does not directly allow for any conclusions on changes in the frequency of storm surges. In that sense it may be of interest to extend the analysis by a type of peak-over-threshold analysis (as was done in Andersen et al. 2015; Antony et al. 2014; Ji et al. 2019).

Finally, where this study is the first attempt to study global surge water levels from satellite radar altimetry, several recommendations for future research were identified. To ensure consistent data availability throughout the considered period, this study did not include synthetic aperture radar (SAR) altimetry from the CryoSat-2 and Sentinel-3 missions. Nonetheless, the inclusion of additional data would likely result in improved accuracy of the estimated MM. Moreover, the high spatial resolution of SAR altimeter data may possibly surpass the need to omit data from sea-ice affected regions, as the smaller footprint allows the retrieval of water level from fractures in the sea ice (Quartly et al. 2018). Similarly, these data are less affected by the contamination from land in coastal regions, hence their use may possibly allow to bridge the gap between the tide gauges and satellite data. However, including these SAR data requires several adaptations of the methodology. Firstly, it would require the use of time-variable scaling factors, as the addition of the SAR data significantly alters the sampling frequency for the last decade compared to the rest of the considered period (as was shown in Fig. 1). Secondly, considering sea-ice affected regions requires tailored processing of the altimeter data and, thirdly, since in these regions only SAR data can be used, it needs to be assessed whether the current record length (13 years) is sufficient for secular analysis. On a similar note, it is recommended to consider the use of publicly available coastal altimeter data sets (e.g., XTrack (Birol et al. 2021)) as this would allow better comparison with the analysis of tide gauge data. However, this requires increased efforts to ensure compatibility between the coastal and open ocean altimeter data sets. Lastly, it may be worthwhile to develop a universal relation between the required scaling and the (space- and time-dependent) data availability, surpassing the need to resort to reanalysis data.

6 Conclusions

The data from eight LRM satellite radar altimeters (1993–2021) have been used to study the temporal and spatial variability in global storm surge water levels. The time-averaged surge water levels were dominated by a zonal pattern, with higher water levels at mid and high latitudes compared to the equatorial region. The highest water levels were observed in the Southern Ocean, northwest Pacific Ocean, northwest Atlantic Ocean, and North Sea. In particular, the surge in water levels in the northern hemisphere was subject to significant annual variability. Overall, the maximum storm surge water levels mainly occurred in the local winter months, that is, except for the tropics where the annual phase showed more local variability. Finally, moderate secular changes of ~ 0.25 cm/year were derived for the $MM_{\frac{1}{6}}$. The derived changes were predominantly negative, except for a few mid-latitude regions with positive changes.

Except for the secular changes, the satellite-derived results were comparable to the information derived from tide gauges, although the tide gauges showed more local variability. The poor correlation for the secular change may be related to the change in water levels being dominated by either a change to tropical or extra-tropical surges. It has been suggested that the satellites may not be able to fully capture the temporal variability in short-lived tropical storms.

Nevertheless, the results provide valuable information on the spatial and temporal variability in storm surge water levels, in particular for regions that are not covered by the many, yet clustered tide gauges. Further analysis with the inclusion of high-frequency (SAR) data and/or the tailored processing of data in coastal and sea-ice affected regions may potentially bridge the remaining gaps between the coast and open ocean.

Acknowledgements This work is part of the research program FAST4NI with project number ALWPP.2017.001, which is (partly) financed by the Dutch Research Council (NWO).

Data availibility The reanalysis data (GTSM) were kindly provided by Deltares, The Netherlands. The GESLA-3 data set was obtained from https://rmets.onlinelibrary.wiley.com/doi/10.1002/gdj3.174 and the satellite radar altimeter data through http://rads.tudelft.nl.

Declarations

Conflict of interest The authors declare no competing interests.

References

Adebisi N, Balogun AL, Min TH, Tella A (2021) Advances in estimating sea level rise: a review of tide gauge, satellite altimetry and spatial data science approaches. Ocean & Coastal Management 208. https://doi.org/10.1016/j.ocecoaman.2021.105632

Andersen OB, Cheng Y, Deng X, Steward M, Gharineiat Z (2015) Using satellite altimetry and tide gauges for storm surge warning. Proceedings of the international association of hydrological sciences 365:28–34. https://doi.org/10.5194/piahs-365-28-2015

Andersen OB, Knudsen P, Stenseng L (2018) A new DTU18 MSS mean sea surface-improvement from SAR altimetry. 25 years of progress in radar altimetry symposium

Antony C, Testut L, Unnikrishnan AS (2014) Observing storm surges in the Bay of Bengal from satellite altimetry. Estuarine, Coastal and Shelf Science 151:131–140. https://doi.org/10.1016/j.ecss.2014.09.012

Beckley B, Ray RD, Zelensky N, Lemoine F, Brown S, Desai S, Mitchum G (2021) Integrated multi-mission ocean altimeter data for climate research TOPEX/Poseidon, Jason-1, 2, & 3 User's Handbook Version 5.1

Bij de Vaate I, Vasulkar AN, Slobbe DC, Verlaan M (2021) The influence of arctic landfast ice on seasonal modulation of the M2 tide. J Geophys Res: Oceans 126, e2020JC016630. https://doi.org/10.1029/2020JC016630

Birol F, Léger F, Passaro M, Cazenave A, Niño F, Calafat FM et al (2021) The x-track/ales multi-mission processing system: new advances in altimetry towards the coast. Adv Space Res 67(8):2398–2415. https://doi.org/10.1016/j.asr.2021.01.049

Butler A, Heffernan JE, Tawn JA, Flather RA, Horsburgh KJ (2007) Extreme value analysis of decadal variations in storm surge elevations. J Marine Syst 67(1–2):189–200. https://doi.org/10.1016/j.jmarsys.2006.10.006

Calafat FM, Wahl T, Tadesse MG, Sparrow SN (2022) Trends in Europe storm surge extremes match the rate of sea-level rise. Nature 603(7903), 841–845. https://doi.org/10.1038/s41586-022-04426-5

Camp J, Roberts M, MacLachlan C, Wallace E, Hermanson L, Brookshaw A, Scaife AA (2015) Seasonal forecasting of tropical storms using the Met Office GloSea5 seasonal forecast system. Quarterly J Royal Meteorol Soc 141(691):2206–2219. https://doi.org/10.1002/qj.2516

Cancet M, Andersen O. Stenseng L, Lyard F, Cotton D, Benveniste J, Schulz A (2015) High resolution tidal modeling in the arctic ocean: needs and upcoming developments. Sentinel-3 for science workshop (Vol 734, p 64)

Cartwright DE, Edden AC (1973) Corrected tables of tidal harmonics. Geophys J R Astron Soc 33:253–264. https://doi.org/10.1111/j.1365-246X.1973.tb03420.x

Cartwright DE, Taylor RJ (1971) New computations of the tide generating potential. Geophys J R Astron Soc 23:45–74. https://doi.org/10.1111/j.1365-246X.1971.tb01803.x

Codiga DL (2020) UTide unified tidal analysis and prediction functions. MATLAB central file exchange. [Software]. https://www.mathworks.com/matlabcentral/fileexchange/46523-utide-unified-tidal-analysis-and-prediction-functions. (Last checked on 10/06/2020)

Dinardo S, Fenoglio-Marc L, Buchhaupt C, Becker M, Scharroo R, Fernandes MJ, Benveniste J (2018) Coastal SAR and PLRM altimetry in German bight and west Baltic Sea. Adv Space Res 62(6):1371–1404. https://doi.org/10.1016/j.asr.2017.12.018

Feng J, Li D, Wang T, Liu Q, Deng L, Zhao L (2019) Acceleration of the extreme sea level rise along the Chinese coast. Earth and Space Science 6(10):1942–1956. https://doi.org/10.1029/2019ea000653

Gori A, Lin N, Xi D, Emanuel K (2022) Tropical cyclone climatology change greatly exacerbates us extreme rainfall-surge hazard. Nat Clim Chang 12(2):171–178. https://doi.org/10.1038/s41558-021-01272-7

Haigh ID, MacPherson LR, Mason MS, Wijeratne EMS, Pattiaratchi CB, Crompton RP, George S (2014) Estimating present day extreme water level exceedance probabilities around the coastline of Australia: tropical cyclone-induced storm surges. Clim Dyn 42(1):139–157. https://doi.org/10.1007/s00382-012-1652-1

Haigh ID, Marcos M, Talke SA, Woodworth PL, Hunter JR, Haugh BS, . . . Thompson P (2022) GESLA version 3: a major update to the global higher-frequency sea-level dataset. [Dataset]. Geoscie Data J. https://doi.org/10.1002/gdj3.174

IPCC (2021) Climate change 2021: the physical science basis. Contribution of Working Group I to the Sixth Assessment Report of the Intergovernmental Panel on Climate Change [Masson-Delmotte V, Zhai P, Pirani A, Connors SL, Péan C, Berger S, Caud N, Chen Y, Goldfarb L, Gomis MI, Huang M, Leitzell K, Lonnoy E, Matthews JBR, Maycock TK, Waterfield T, Yelekç O, Yu R, Zhou B (eds)]. Cambridge University Press. https://doi.org/10.1017/9781009157896

Izaguirre C, Méndez FJ, Menéndez M, Losada IJ (2011) Global extreme wave height variability based on satellite data. Geophys Res Lett 38:(10). https://doi.org/10.1029/2011GL047302

Ji T, Li G, Zhang Y (2019) Observing storm surges in China's coastal areas by integrating multi-source satellite altimeters. Estuarine, Coastal and Shelf Science 225. https://doi.org/10.1016/j.ecss.2019.05.006

Kleinherenbrink M, Lindenbergh R, Ditmar P (2015) Monitoring of lake level changes on the Tibetan Plateau and Tian Shan by retracking Cryosat SARIn waveforms. J Hydrol 521:119–131. https://doi.org/10.1016/j.jhydrol.2014.11.063

Knapp KR, Diamond HJ, Kossin JP, Kruk MC, Schreck CJ (2022) International best track archive for climate stewardship (IBTrACS) Project, Version 4. [Dataset]. NOAA National Centers for Environmental Information. https://doi.org/10.25921/82ty-9e16

Lobeto H, Menendez M, Losada IJ (2018) Toward a methodology for estimating coastal extreme sea levels from satellite altimetry. J Geophys Res: Oceans 123(11):8284–8298. https://doi.org/10.1029/2018JC014487

Marcos M, Woodworth PL (2018) Changes in extreme sea levels. CLIVAR Exchanges 16(1):20–24

McGranahan G, Balk D, Anderson B (2007) The rising tide: assessing the risks of climate change and human settlements in low elevation coastal zones. Environment and urbanization 19(1):17–37. https://doi.org/10.1177/0956247807076960

Méndez FJ, Menéndez M, Luceño A, Losada IJ (2007) Analyzing monthly extreme sea levels with a time-dependent GEV model. J Atmos Ocean Technol 24(5):894–911. https://doi.org/10.1175/JTECH2009.1

Menéndez M, Woodworth PL (2010) Changes in extreme high water levels based on a quasi-global tide-gauge data set. J Geophys Res: Oceans, 115 (C10). https://doi.org/10.1029/2009JC005997

Muis S, Verlaan M, Winsemius HC, Aerts JC, Ward PJ (2016) A global reanalysis of storm surges and extreme sea levels. Nat Commun 7(1):1–12. https://doi.org/10.1038/ncomms11969

Naeije MC (2022) Radar altimeter database system. [Data archive]. http://rads.tudelft.nl

NSIDC (2022) Sea ice index, version 3 (G02135) [Dataset]. NOAA National Centers for Environmental Information. https://nsidc.org/data/g02135/versions/3#anchor-2

Oppenheimer M, Glavovic B, Hinkel J, van de Wal R, Magnan AK, Abd-Elgawad A, . . . Sebesvari Z (2019) Sea level rise and implications for low lying islands, coasts and communities. In: IPCC Special Report on the Ocean and Cryosphere in a Changing Climate [Pörtner H-O, Roberts DC, Masson- Delmotte V, Zhai P, Tignor M, Poloczanska E, Mintenbeck K, Nicolai M, Okem A, Petzold J, Rama B, Weyer N (eds)], 321–445

Quartly GD, Rinne E, Passaro M, Andersen OB, Dinardo S, Fleury S, . . . others (2018) Review of radar altimetry techniques over the arctic ocean: recent progress and future opportunities for sea level and sea ice research. The Cryosphere Discussions, 1–51. https://doi.org/10.5194/tc-2018-148

Rashid M, Wahl T (2020) Predictability of extreme sea level variations along the U.S. Coastline. J Geophys Res: Oceans 125:(9). https://doi.org/10.1029/2020jc016295

Resio DT, Westering JJ (2008) Modeling the physics of storm surges. Physics Today 61:33–38. https://doi.org/10.1063/1.2982120

Rhines P (2001) Mesoscale eddies. Steele JH (ed), Encyclopedia of ocean sciences (p 1717-1730). Oxford: Academic Press. https://doi.org/10.1006/rwos.2001.0143

Tran N, Dibarboure G, Picot N, Féménias P (2018) Improving the continuity of the Jason SSB time-series. In OSTST meeting, September

Von Storch H, Woth K (2008). Storm surges: perspectives and options. Sustain Sci 3(1):33–43. https://doi.org/10.1007/s11625-008-0044-2

Wahl T, Haigh ID, Nicholls RJ, Arns A, Dangendorf S, Hinkel J, Slangen AB (2017) Understanding extreme sea levels for broad-scale coastal impact and adaptation analysis. Nat Commun 8(1):1–12. https://doi.org/10.1038/ncomms16075

Wahr JM (1985) Deformation induced by polar motion. J Geophys Res 90(B11):9363–9368. https://doi.org/10.1029/JB090iB11p09363

Wang X, Verlaan M, Apecechea MI, Lin HX (2021) Computation-efficient parameter estimation for a high-resolution global tide and surge model (GTSM). J Geophys Res: Oceans 126 ,e2020JC016917. https://doi.org/10.1029/2020JC016917

Weisse R, Bellafiore D, Menéndez M, Méndez F, Nicholls RJ, Umgiesser G, Willems P (2014) Changing extreme sea levels along European coasts. Coast Eng 87(1):1–14. https://doi.org/10.1016/j.coastaleng.2013.10.017